

## Water Dynamics in Polyacrylamide Hydrogels

Chang Yan<sup>†‡</sup>, Patrick L. Kramer<sup>†</sup>, Rongfeng Yuan and Michael D. Fayer<sup>\*</sup>

Department of Chemistry  
Stanford University, Stanford, CA 94305

<sup>†</sup>C.Y. and P.L.K. contributed equally to this work

<sup>‡</sup>Current address: Department of Chemistry, University of California, Berkeley, CA 94720

<sup>\*</sup>Corresponding Author. Email: fayer@stanford.edu. Phone: 650 723-4446.

### Supporting Information

#### A. Methods for linear IR absorption and time-resolved nonlinear IR spectroscopy

Fourier-transform IR (FTIR) spectra were recorded on a Thermo Scientific Nicolet 6700 FTIR spectrometer with a resolution of  $0.5\text{ cm}^{-1}$ . For O-D hydroxyl spectra in hydrogel samples, background absorption due to H<sub>2</sub>O and PAAm was removed in two steps. The majority of the background, contributed by H<sub>2</sub>O, was subtracted using the spectrum of pure H<sub>2</sub>O as the first step. Some residual absorption blue of the hydroxyl (O-D) stretch remained from the PAAm fibers. The FTIR spectrum of a low-concentration hydrogel (10% PAAm) containing only H<sub>2</sub>O was background subtracted, resulting in the isolated polymer spectrum. This polymer spectrum was subtracted from the O-D absorption spectrum in the second step of background correction. For SeCN<sup>-</sup> spectra, D<sub>2</sub>O background absorption was subtracted using a spectrum of pure D<sub>2</sub>O. The background spectra of hydrogels containing D<sub>2</sub>O do not differ from pure D<sub>2</sub>O in the C-N stretch spectral region.

The ultrafast IR measurements of hydrogels were performed on two different IR laser systems at a temperature of  $297.0 \pm 0.3\text{ K}$ . For the measurements on 5% HOD in hydrogels, the broadband mid-infrared (MIR) source and time resolved IR spectrometer have been described in detail previously.<sup>1,2</sup> Briefly, a relatively short pulse Ti:Sapphire regenerative amplifier (1 or 2 kHz, 45 fs FWHM, 800 nm output) pumped an optical parametric amplifier (OPA) to produce 60 fs FWHM, 4  $\mu\text{J}$  MIR pulses centered at  $2510\text{ cm}^{-1}$  with a bandwidth of about  $230\text{ cm}^{-1}$ . These short pulses with large bandwidth are required to cover the very broad hydroxyl (O-D) absorption band. 2D IR measurements used a non-collinear box-CARS geometry in which the direction, timing, polarization, and intensity of the three excitation pulses, signal, and local oscillator (LO) are independently controllable.<sup>3-5</sup> The time delay between pulses one and two is scanned to generate an interferogram, while the second to third pulse time delay is the waiting

time,  $T_w$ . 2D IR experiments on HOD were done with the same polarization for the 3 input pulses and the echo signal pulse, i.e., the  $\langle XXXX \rangle$  polarization configuration. PSPP measurements were conducted with a strong pump pulse and weak probe pulse, and are otherwise the same as described for the pulse-shaping system below. Vibrational population relaxation of the O-D stretch in bulk water and similarly water-rich environments results in a transient heating signal originating from the breaking of hydrogen bonds.<sup>6,7</sup> This isotropic contribution to the PSPP data was removed following a well-documented procedure<sup>6,7</sup> to recover the pure lifetime decays for the O-D stretch of HOD in the PAAm gels.

For hydrogels that contain  $\text{SeCN}^-$  as the probe, experiments were carried out with an IR Fourier-domain pulse-shaping system. Details of this system have been described previously.<sup>8,9</sup> The IR output from the OPA is a 3 kHz pulse train with a pulse energy of  $\sim 30 \mu\text{J}$ . The IR spectrum was centered at  $2075 \text{ cm}^{-1}$  with a bandwidth of  $100 \text{ cm}^{-1}$ , giving a duration of  $\sim 160 \text{ fs}$ . The IR beam was split into a pump beam and a probe beam (90:10). The pump beam passed through an acousto-optic modulator (AOM) that generated two pulses separated by time  $\tau$  for the 2D IR measurements and a single pulse for the pump-probe experiments. The probe pulse (corresponding to pulse 3 in the echo experiments) was delayed by a mechanical delay line to scan the time between pump and probe, denoted  $T_w$  in the 2D IR and  $t$  in the PSPP experiments. For the PSPP experiments, the probe beam polarization was set horizontal ( $0^\circ$ ) and the pump beam polarization was set  $+45^\circ$ . After the sample, the probe beam passed through a motorized resolving polarizer that was alternated between  $+45^\circ$  or  $-45^\circ$  so that the components of the probe (and thus pump-probe signal) parallel ( $S_{\parallel}$ ) and perpendicular ( $S_{\perp}$ ) were obtained.<sup>10</sup> Then the probe beam entered a spectrograph with horizontal polarization after a final polarizer and was detected with a 32-pixel MCT array. The parallel and perpendicular PSPP signals are described by:

$$\begin{aligned} S_{\parallel}(t) &= P(t)(1 + 0.8C_2(t)) \\ S_{\perp}(t) &= P(t)(1 - 0.4C_2(t)). \end{aligned} \tag{S1}$$

The population decay,  $P(t)$ , is isolated using equation (1) in the main text. Rotational motions are extracted from through the anisotropy, equation (2) in the main text.

For 2D IR measurements using the pulse-shaping system, the optical alignments were the same as the PSPP experiments. The AOM split each pump pulse into pulse 1 and pulse 2 which

were collinear but delayed by the period  $\tau$  and with controlled varying phase. The probe pulse (pulse 3) stimulated the emission of echo pulse travelling collinearly with the probe pulse. The probe pulse therefore also served as the LO pulse. For each 2D IR spectrum acquired at a certain  $T_w$ ,  $\tau$  was scanned by the AOM to generate the interferograms recorded on the array pixels. In the same manner as in the PSPP measurements, the polarization of pulse 1 and 2 is either  $45^\circ$  or  $-45^\circ$  relative to the horizontal pulse 3 during the measurements. The measured  $\langle XXXX \rangle$  and  $\langle XXY Y \rangle$  2D IR spectra were transformed as  $\langle XXXX \rangle + 2\langle XXY Y \rangle$  into the isotropic 2D IR spectra used for spectral diffusion analysis.<sup>11,12</sup> Unlike for HOD as the vibrational probe, the 2D IR spectra are in the isotropic polarization configuration. The reorientation measurements revealed two distinct populations for the anionic probe:  $\text{SeCN}^-$  in the core of the nanopools and associated with polymer fibers. The isotropic 2D IR observable eliminates orientational relaxation from influencing relative amplitudes contributing to the 2D IR spectra.

### **B. Wobbling-in-a-cone correlation functions, cone angles, and diffusion constants**

The wobbling-in-a-cone model with a hard cone potential<sup>12-16</sup> has found great success in quantitatively describing restricted orientational diffusion observed in pump-probe<sup>2,12,17,18</sup> and fluorescence<sup>13,14,19</sup> anisotropy decay, NMR Overhauser enhancement,<sup>15,20</sup> and time-domain optical Kerr effect<sup>21-24</sup> measurements. In this section we provide some additional details on this highly informative model.

The key piece of information obtained from the anisotropy observable is the second order Legendre polynomial orientational correlation function:

$$C_2(t) = \langle P_2(\vec{\mu}(t) \cdot \vec{\mu}(0)) \rangle, \quad (\text{S2})$$

where  $P_2$  is the second Legendre polynomial and  $\vec{\mu}(t)$  is the time dependent transition dipole orientation, a unit vector. If  $C_2$  is found to decay to zero in the infinite-time limit, then the orientational motion samples all directions on a long enough timescale. However, restrictions on the range of orientational motion, such as attachment of the probe to an immobile surface, can cause  $C_2$  to decay to an offset. This offset is given by  $S_2^2$ , the square of a generalized order parameter:

$$S_2 = \langle P_2(\cos \theta) \rangle = \int d\Omega P_2(\cos \theta) p_{\text{eq}}(\theta), \quad (\text{S3})$$

where  $p_{\text{eq}}(\theta)$  is the equilibrium probability density of transition dipole polar angles (assumed azimuthally around the  $z$ -axis) and  $\Omega$  refers to the angular coordinates  $(\theta, \phi)$ .<sup>15</sup>

This order parameter alone provides model-free information about the confining potential, but much better understanding of both the structural features of the restriction and the dynamics within the confining potential can be gained by introducing a particular model. The hard cone model is both conceptually clear and allows for some analytical results, as shown by Lipari and Szabo.<sup>15</sup> In this model, the unique symmetry axis of the probe, which is assumed to be coincident with the transition dipole direction and thus the bond axis, undergoes free diffusion within a cone around the  $z$ -axis of half angle  $\theta_0$ . There is equal probability of finding any value of the polar angle  $\theta$  within the cone, and zero probability of it appearing outside:  $p_{\text{eq}}(\theta) = 0$  for  $\theta > \theta_0$ .

The model inputs are thus a hard cone half angle  $\theta_0$  and orientational diffusion constant  $D_w$  for the free rotational diffusion within the cone. It is straightforward to calculate the order parameter with this model. Defining  $x_0 = \cos \theta_0$ , we have:

$$S_2 = \frac{x_0(1+x_0)}{2}, \quad (\text{S4})$$

which was also given in the form of equation (4) in the main text. An excellent analytical approximation to the full orientational correlation function is available,<sup>15</sup> taking the form of a single exponential decay to an offset, which is the squared order parameter:

$$C_2(t) = S_2^2 + (1 - S_2^2) \exp(-t / \tau_c). \quad (\text{S5})$$

The effective wobbling time constant,  $\tau_w$ , depends on both the diffusion constant and the cone angle;<sup>15</sup> it is given by:

$$\begin{aligned} \tau_c D_w (1 - S_2^2) = & - \frac{x_0^2 (1 + x_0)^2 (\log[(1 + x_0) / 2] + (1 - x_0) / 2)}{2(1 - x_0)} \\ & + \frac{(1 - x_0) (6 + 8x_0 - x_0^2 - 12x_0^3 - 7x_0^4)}{24}. \end{aligned} \quad (\text{S6})$$

If the model inputs  $\theta_0$  and  $D_w$  are known, the orientational correlation function (S5) can be constructed. More importantly, when the orientational correlation function is determined through a fit to experimental data of the form (S5), we can straightforwardly solve the reverse problem to

obtain the model characteristic parameters  $\theta_0$  and  $D_w$  from the fit parameters  $S_2^2$  and  $\tau_c$  using (S4) and (S6).  $S_2$  directly gives the cone angle, and then  $\theta_0$  and  $\tau_c$  are used to determine  $D_w$ .

In the main text (Sections II.B,C and Table I), the anisotropy decays of HOD in H<sub>2</sub>O and SeCN<sup>-</sup> in D<sub>2</sub>O, in hydrogels of various PAAm concentration, are analyzed. Results for  $\tau_c$  and  $\theta_c$  are reported; these two give good descriptions of the observable decay rates and structural constraints, respectively. To compare the rates at which diffusion in the cones is actually occurring, however, the diffusion constant is the more relevant parameter. Data from the fits that is useful for the calculation from Table I (main text) are reproduced in Table S1. The wobbling-in-a-cone diffusion constants  $D_w$  were calculated for HOD and SeCN<sup>-</sup> in bulk solution and the various concentration hydrogels. We report the inverse diffusion constant, or diffusion timescale,  $D_w^{-1}$  in Table S1 for comparison in more convenient units.

### **C. Estimation of water pool size in PAAm hydrogels for model distributions and comparison to reverse micelles**

In examining the structural and rotational dynamics of vibrational probes (HOD and SeCN<sup>-</sup>) in the restricted hydrogel networks, it can be helpful to consider the relationship between the PAAm concentration  $T$  (percent weight / volume) and the average water pore dimensions in which either probe molecule can reside. In the present section we consider two limiting cases of the pore distribution in PAAm hydrogels. The first is a model originally derived by Ogston which assumes a completely random distribution of long polymer fibers in a suspension.<sup>25</sup> The Ogston model and its extensions have a long history of use in examining the physical properties of hydrogels and relating them to performance in electrophoresis, yielding a well-known  $T^{-1/2}$  dependence of pore size on polymer concentration.<sup>26-29</sup> The complete randomness of the distribution yields a relatively small average pore diameter. In the opposite limit, we consider a model of a highly organized lattice of polymer fibers. Assuming a three-dimensional cubic lattice, the average pore size (or polymer fiber spacing) is straightforward to calculate. This gives an upper bound on the pore diameter as the highly organized polymer network allows for greater spacing between the fibers.

Given these relationships of polymer concentration to water pool dimensions in the hydrogel, we may compare to a different system of confined water: that in reverse micelles. Reverse micelles have been extensively studied in terms of both their structure and the dynamics

of the water inside. The spherical micelle diameter is simply related to the ratio of water to surfactant head groups, allowing comparison to the characteristic hydrogel pore sizes we examine in the following.

For Ogston's uniform random fiber suspension model,<sup>25</sup> we assume identical straight fibers of length  $2L$  (a distance  $L$  to each end from the fiber center) with a uniform average number density  $\nu$  of fiber centers per  $\text{cm}^3$ . We further assume the fiber radius  $r$  is finite but small enough compared to the fiber length that it does not affect the distribution of fiber centers or orientations. In an isotropic suspension, all fiber orientations are equally probable. The size of a pore or space is defined by taking any given point in the medium and determining the largest sphere that can be constructed from this center before making contact with a fiber. This distance from a chosen origin to the nearest fiber is denoted  $D$ , which defines the pore radius.

Ogston determined the probability distribution of  $D$  in general using only the above assumptions.<sup>25</sup> The results are considerably simplified with one further approximation also introduced by Ogston: that the values of interest for  $D$  (i.e., those with significant probability) satisfy  $D \ll L$ , which is likely to hold for large  $L$  at moderate concentrations  $\nu$ . The probability density of  $D$  was found to be:

$$\frac{dP}{dD} = 4\pi\nu LD \exp(-2\pi\nu LD^2), \quad (\text{S7})$$

from which the mean value of  $D$  is found as:

$$\langle D \rangle = (8\nu L)^{-1/2}. \quad (\text{S8})$$

Ogston observed the extremely useful fact that equations (S7) and (S8) do not depend on  $\nu$  and  $L$  individually, but rather their product, which is proportional to the total length of fiber per unit volume.<sup>25</sup> Defining  $\alpha$  as the length of fiber per  $\text{cm}^3$ , we have  $\alpha = 2L\nu$  and thus  $\langle D \rangle = (4\alpha)^{-1/2}$ .

Given the concentration of polymer in mass per unit volume,  $C_m$  in  $\text{g}/\text{cm}^3$  (so that  $T(\%) = 100 \times C_m$ ), the polymer fiber radius  $r$ , the molar volume contributed per monomer unit  $V_m$ , and the monomer unit molar mass  $M_w$ , we can calculate the length of fiber per unit volume  $\alpha$  and thus the mean pore radius  $\langle D \rangle$ . The volume of polymer per  $\text{cm}^3$  of liquid suspension is

$$V_p = \frac{V_m C_m}{M_w}. \quad (\text{S9})$$

The cross sectional area of a polymer fiber is given simply by  $A_c = \pi r^2$ . Thus the length of fiber per volume of suspension is

$$\alpha = \frac{V_p}{A_c} = \frac{V_m C_m}{\pi r^2 M_w}, \quad (\text{S10})$$

from which it follows that the mean pore radius is

$$\langle D \rangle = (4\alpha)^{-1/2} = \frac{\sqrt{\pi}}{2} r \sqrt{\frac{M_w}{V_m C_m}}. \quad (\text{S11})$$

For the later comparisons, it will be more useful to evaluate the mean pore diameter,

$$d = 2\langle D \rangle = \sqrt{\pi} r \sqrt{\frac{M_w}{V_m C_m}}. \quad (\text{S12})$$

The expected  $C_m^{-1/2}$  dependence appears in (S12).

For the second model, we assume a three dimensional lattice of polymer fibers. A cubic lattice is considered for simplicity; other lattice shapes would be expected to give similar, but not identical, results. The cubic unit cell is illustrated in Figure S5. The length of each edge is  $l$ , giving a box volume of  $V = l^3$ . The polymer fiber radius is  $r$  as introduced above. This perfectly organized hydrogel model contains three intersecting polymer fibers, modeled as cylinders, whose axes are orthogonal. The distance between each adjacent parallel fiber is clearly  $l$ . Thus  $l$  is the characteristic “diameter” or length scale of the water pore in this network structure, which can be compared with  $d$  in (S12).

To calculate  $l$ , we observe that there is a definite polymer mass contained in a cell of this given length scale. This mass  $m$  per cell volume  $V$  must be  $C_m$ , which is known. The total volume of the three cylindrical fibers is

$$V_T = 3\pi r^2 l. \quad (\text{S13})$$

Now, given the molar mass and molar volume per monomer unit, we obtain the mass of polymer per unit cell:

$$m = \frac{V_T M_w}{V_m} = \frac{3\pi r^2 l M_w}{V_m}. \quad (\text{S14})$$

To match the experimental polymer concentration, we must have:

$$C_m = \frac{m}{V} = \frac{m}{l^3} = \frac{3\pi r^2 M_w}{V_m l^2}. \quad (\text{S15})$$

Solving (S15) for  $l$ , we obtain the desired expression for the cubic cell length:

$$l = \sqrt{3\pi} r \sqrt{\frac{M_w}{V_m C_m}}. \quad (\text{S16})$$

This result is larger than for the random fiber distribution result  $d$  in (S12) by a factor of  $\sqrt{3}$ , but otherwise has identical form.

The expressions (S12) and (S16) for  $d$  and  $l$ , respectively, are the distances between the centers of polymer fibers which define the pore. When the polymer radius  $r$  is finite, it also restricts the available pore space. To account for this, as suggested by Ogston, we can subtract the fiber diameter of  $2r$  from the diameters  $d$  and  $l$  to obtain the actual size of the water pore in each of the models.<sup>25</sup> Thus we have

$$d_w = \sqrt{\pi} r \sqrt{\frac{M_w}{V_m C_m}} - 2r \quad (\text{S17})$$

and

$$l_w = \sqrt{3\pi} r \sqrt{\frac{M_w}{V_m C_m}} - 2r \quad (\text{S18})$$

for the random fiber suspension (Ogston) and lattice model water pool diameters, respectively.

In order to evaluate the expressions for  $d_w$  and  $l_w$  as a function of the PAAm concentration  $C_m$ , we need the parameters characterizing this polymer in aqueous solution or suspension. The molar mass for the acrylamide monomer is  $M_w = 71.08$  g/mol. For the definition of polymer volume, the most appropriate choice is the Van der Waal's volume, representing the space occupied by the polymer fibers in solution. We have for PAAm,  $V_m = 38.15$  cm<sup>3</sup>/mol as the Van der Waal's volume per mole of acrylamide monomer.<sup>30</sup> The final required property, the PAAm fiber radius  $r$ , is less straightforward to obtain as it depends on the exact synthesis conditions of the crosslinked hydrogel network. If the fibers were single-monomer thick fibers, then one could simply use the radius of an assumed spherical monomer Van der Waal's volume:

$$r = \left( \frac{3V_m}{4\pi N_A} \right)^{1/3} = 0.247 \text{ nm} ,$$

with  $N_A$  Avogadro's number. However, the fiber radius depends on the extent of PAAm crosslinking. Through molecular-sieve chromatographic separations on various proteins of known hydrodynamic radii in granulated PAAm gel, Fawcett and Morris found a simple relation between the fiber thickness and the cross linker concentration  $C$  in weight percent of total monomer.<sup>28</sup> For  $C$  less than 10%, as is typical, the fiber radius is:

$$r \text{ (nm)} = 0.50 + 0.10C \text{ (}\% \text{)} . \quad (\text{S19})$$

The concentration for all samples was  $C = 3.3\%$  (main text, Section II.A), so we obtain  $r = 0.83$  nm. This value of  $r$ , slightly more than three monomer units worth, is certainly much smaller than the fiber length. Thus the assumption in the Ogston model that the finite radius does not influence the fiber distribution should hold.

Given the parameters obtained above, the calculated values of  $d_w$  and  $l_w$  are displayed in Table S2 as a function of PAAm concentration,  $T$ . For hydrogels at or above 10% PAAm, both the lower bound,  $d_w$ , and upper bound,  $l_w$ , water pore diameters are below 10 nm, supporting the experimental observations of significant dynamical slowdown resulting from the confinement of the H-bonded water pool, which begins at PAAm concentrations of about 10%.

We now compare the mean pore sizes evaluated above for the spaces in PAAm hydrogels to the water pool sizes of reverse micelles (RMs). A mixture of water and surfactant with a certain ratio  $w_0$  of water molecules per surfactant head group will self-organize in nonpolar solvents into typically spherical RMs of a particular, nearly monodisperse, size over a range of  $w_0$  values.<sup>31,32</sup> For RMs based on Aerosol-OT (AOT, sodium di-2-ethylhexylsulfosuccinate) in isooctane, a simple relation between water to surfactant ratio  $w_0$  and water pool diameter has been established through light scattering and viscosity methods. Using a surfactant length of 1.2 nm for AOT, Kinugasa et. al. found a simple linear relationship that describes multiple sets of RM size measurements:

$$d_m \text{ (nm)} = 0.29w_0 + 1.1, \quad (\text{S20})$$

valid for  $w_0$  between 2 and 20.<sup>31</sup> Thus, given a water pool size as calculated with our PAAm hydrogel models above, we can calculate the equivalent  $w_0$  for a RM from:

$$w_0 = \frac{d_m \text{ (nm)} - 1.1}{0.29}. \quad (\text{S21})$$

Calculated values of  $w_0$  using (S21) for the hydrogel concentrations examined in the present

work are shown in Table S2. We use an equivalent  $d_m^{\text{gel}}$  that is the mean of  $l_w$  and  $d_w$ .

Intermediate length scales are characteristic of a hydrogel framework with a mix of disorder and more lattice-like arrangements. The values appear mostly within the range of applicability of equations (S20) and (S21), though for  $d_m = 10.6$  nm,  $w_0 = 33$  is somewhat too high of an estimate.<sup>32-34</sup>

In comparing hydrogel and RM confinement of water, it is also worth considering the geometric fraction of water that is adjacent to the interface, as was calculated by Moilanen, et. al. for several large RMs previously.<sup>33</sup> For reverse micelles, the radius of the water pool is  $r_m = d_m / 2$ , with  $d_m$  given by Eq. (S20). We take the thickness of a single water hydration shell, present at the interface adjacent to surfactant molecules, to be  $\rho = 0.285$  nm.<sup>35</sup> Then, the radius of the “core” water pool is  $r_c = r_m - \rho$ . The volume of the interfacial water “shell”,  $V_s$  is simply the volume of the total water sphere,  $V$ , minus the volume of the core water sphere,  $V_c$ . The geometric fraction of interfacial water is given by:

$$f_s^{\text{RM}} = \frac{V_s}{V} = \frac{V - V_c}{V} = \frac{\rho(\rho^2 - 3\rho r_m + 3r_m^2)}{r_m^3}. \quad (\text{S22})$$

The calculation for RMs was straightforward because there is a clear geometry for each (identical) water pool in solution.

In the hydrogels, the water pool is continuous, and rather than knowing its size, we have direct access to the polymer volume fraction, in Eq. (S9) for  $V_p$ . The calculation of interfacial water fraction is independent of the organization of polymer fibers in the suspension. With reference to Figure S5, consider a cylindrical fiber of PAAm of radius  $r$ . The volume per unit length is  $\pi r^2$ . Interfacial water consists of a shell around this cylinder of thickness  $\rho$ . The total cylinder volume per unit length of fiber is  $\pi(r + \rho)^2$ . Then the volume fraction of interfacial water,  $V_s$ , can be found from the ratio of water shell to fiber volume, as we know  $V_p$ :

$$V_s = \frac{\pi(r + \rho)^2 - \pi r^2}{\pi r^2} V_p = \frac{\rho(\rho + 2r)}{r^2} V_p. \quad (\text{S23})$$

The volume fractions  $V_s$  and  $V_p$  are out of a total value of unity for the entire polymer fiber suspension. Thus the volume fraction of “bulk” water,  $V_b$ , is known from  $V_p + V_s + V_b = 1$ . Here “bulk” refers to all water not directly against the polymer fiber interface, not to imply that its dynamics are necessarily bulk-like. The volume fraction of all water in the suspension is clearly  $V_s + V_b = 1 - V_p$ . Finally, the geometric fraction of interfacial water out of all the water for polymer fiber suspensions is:

$$f_s^{\text{gel}} = \frac{V_s}{V_s + V_b} = \frac{\rho(\rho + 2r)}{r^2} \frac{V_p}{1 - V_p} = \frac{\rho(\rho + 2r)}{r^2} \frac{1}{V_p^{-1} - 1}. \quad (\text{S24})$$

For sufficiently small  $V_p$ , the approximation

$$\frac{V_p}{1 - V_p} \approx V_p \times (1 + V_p) = V_p + V_p^2 \approx V_p$$

gives a linear dependence of interfacial water fraction on polymer volume fraction, as we observed for the polymer fiber-associated  $\text{SeCN}^-$  probe in the main text. The approximate linear relation is easily calculated as:  $f_s^{\text{gel}} \approx 0.43 \times C_m$ . A slope of 0.44 was found experimentally for the fraction of fiber-associated  $\text{SeCN}^-$  as a function of polymer mass fraction. This provides additional justification for the values of  $r$  and  $\rho$  used here.

The interfacial water fractions were calculated for the hydrogels and are given in Table S2. These values of  $f_s^{\text{gel}}$  depend only on the polymer concentration and not the particular organization of fibers, i.e., the random chain versus lattice models. Using the equivalent diameter  $d_m^{\text{gel}}$  that was associated with a RM size, we also calculated the interfacial water fraction that would exist in this hypothetical reverse micelle. These values of  $f_s^{\text{RM}}$  are also displayed in Table S2.

Moilanen et. al. extensively analyzed the vibrational relaxation and rotational dynamics of HOD in AOT reverse micelles formed in isoctane at a range of  $w_0$  values spanning from the smallest possible RMs to large RMs containing considerable bulk water.<sup>33,34</sup> The results are summarized in Table S3. The vibrational lifetime relaxation appeared as two exponentials for larger RMs, signifying two distinct dynamical ensembles. For the smaller RMs, only a single lifetime could be found, illustrating a transition to collective dynamics of the entire water pool.

From the very large RMs at  $w_0 = 37$  through the transition point at  $w_0 = 10$ , a bulk-like “core” component with a shorter lifetime and faster reorientation appeared alongside a “shell” component, water molecules at the interface. The shell population had a longer lifetime and very slow orientational relaxation for all large and intermediate RMs (Table S3).<sup>33,34</sup> Below the  $w_0 = 10$  RM, at values of 5 and 2, only a single, highly perturbed water environment remains, with slightly slower orientational relaxation at  $w_0 = 5$  compared to the shell of larger RMs, and extremely slow relaxation in the smallest RM,  $w_0 = 2$ .

#### D. Calculation of the complete FFCF from the CLS and absorption lineshape

In 2D optical spectroscopy, the center line slope (CLS) method allows for extremely robust extraction of the normalized, time-dependent part of the frequency-frequency correlation function,  $C(t) = \langle \delta\omega(t)\delta\omega(0) \rangle$ , where  $\delta\omega(t) = \omega(t) - \langle \omega \rangle$  is the instantaneous frequency fluctuation around the average value  $\langle \omega \rangle$ .<sup>36-38</sup> We make use of the CLS- $\omega_3$  formulation<sup>37</sup> in particular: slices of the 2D spectrum are taken parallel to the vertical  $\omega_3$  (or  $\omega_m$ ) axis and the position of the maximum value of this slice is determined. The center line is constructed by plotting the position of the max in  $\omega_3$  as a function of the slice value in  $\omega_1$  (or  $\omega_r$ ). Center lines are illustrated in the 2D IR spectra of HOD in hydrogels with 5% and 40% PAAm in Figure S6. The slope of this line is defined as the CLS, beginning from a theoretical value of unity for complete correlation of initial and final frequencies, and decaying to a value of zero at long waiting times for completely uncorrelated initial and final frequencies. It has been shown that the CLS technique retrieves the correct decay function despite the presence of background distortions, excited state absorption peaks (e.g., the 1-2 transition which often partially overlaps the 0-1 peak for ground state bleach and stimulated emission), and phasing error (for experiments done in non-collinear geometries).

We typically consider multi-exponential FFCFs, with explicit inclusion of a homogeneous component, of the form:

$$C(t) = \frac{\delta(t)}{T_2} + \sum_k \Delta_k^2 \exp(-t / \tau_k), \quad (\text{S25})$$

where  $\Delta_k$  is the contribution (in standard deviation of a Gaussian line shape) of process  $k$  to the inhomogeneous broadening.  $T_2$  is the total homogeneous dephasing time, with contributions

from pure dephasing due to extremely fast fluctuations (completely motionally narrowed processes with  $\Delta_k \tau_k \ll 1$ , giving a pure dephasing linewidth of  $\Gamma^* = \Delta_k^2 \tau_k / \pi$ ), vibrational lifetime decay, and orientational relaxation of the transition dipole moment. With pure dephasing time constant  $T_2^* = 1 / (\pi \Gamma^*)$ , vibrational lifetime  $T_1$ , and integrated second order rotational correlation time  $T_{or}$ , the total dephasing time is given by:

$$\frac{1}{T_2} = \frac{1}{T_2^*} + \frac{1}{2T_1} + \frac{1}{3T_{or}}. \quad (\text{S26})$$

The homogeneous linewidth is  $\Gamma = 1 / (\pi T_2)$ , which is the FWHM of the Lorentzian lineshape.

The CLS is a robust and easily obtained observable,<sup>37,38</sup> but we pay the price of losing direct knowledge of  $T_2$  (or  $\Gamma$ ) and the scale of the frequency fluctuations,  $\Delta_k$ , if we analyze the CLS alone.

Two methods are available to recover the complete FFCF using the CLS and some auxiliary information. The first is well-documented and was described along with the CLS procedure initially.<sup>36,37</sup> In this case we require the linear absorption lineshape and the CLS decay (fit and data points). The width of the linear absorption encodes the scale of both the inhomogeneous and homogeneous broadening; the CLS decay, on the other hand, describes how this linewidth is distributed. Diagrammatic perturbation theory is used to calculate the linear absorption spectrum from the complete FFCF. A simultaneous fit of the calculated linear absorption to the experimental FTIR spectrum and of the normalized FFCF (disregarding the homogeneous contribution) to the experimental CLS decay, while varying the scale of the  $\Delta_k$  and  $T_2$ , allows the complete FFCF to be determined. This method gives excellent convergence for symmetric lineshapes and even slightly asymmetric lineshapes such as those of HOD in H<sub>2</sub>O (Figure 1), and was used for HOD in bulk water and in hydrogels at all PAAM concentrations.

However, for the SeCN<sup>-</sup> anion in water (D<sub>2</sub>O), the large red-side tail due to significant non-Condon effects (stronger transition dipole moment for more weakly H-bonded absorbers on the red side)<sup>39</sup> causes poor convergence of the above method and inconsistent FFCF determination. For the SeCN<sup>-</sup> lineshapes in bulk D<sub>2</sub>O and varying concentration of PAAM in the hydrogels, another method was used that was developed for a previous detailed study by Yamada et. al. on the SeCN<sup>-</sup> lineshape and dynamics in pure water.<sup>40</sup>

In this method, we use the fit to the experimental CLS decay, the CLS data point for one chosen waiting time  $T_w$  (typically the earliest available point for best results), and the FWHM,  $w$ , calculated directly from the experimental FTIR absorption spectrum (i.e., not from a fit). Assuming a Voigt line shape of width  $w$  (FWHM), Lorentzian (homogeneous) and Gaussian (inhomogeneous) widths are calculated for range of ratios of homogeneous to inhomogeneous broadening. Diagrammatic perturbation theory is used this time to calculate 2D spectra at a fixed  $T_w$  while varying the FFCF parameters in equation (S25) for the range of homogeneous and inhomogeneous widths chosen. The CLS is taken for each of these calculate spectra and compared to the experimental CLS value at this waiting time. The ratio of the homogeneous and inhomogeneous linewidths for which the actual CLS value is reproduced is thus the correct one, allowing the full FFCF to be calculated. 2D spectra are calculated as a function of waiting time for this complete FFCF and compared to the experimental CLS decay as a consistency check, with good agreement found for bulk water and all the PAAm concentrations we considered.

### **E. Frequency-dependent pump-probe analysis of SeCN<sup>-</sup>**

In Figure S8, the population relaxation curves of PAAm gels with  $T = 5\%$  and  $40\%$  are displayed at three different frequencies: close to the peak center at  $2073 \text{ cm}^{-1}$ , red side to the peak center at  $2065 \text{ cm}^{-1}$ , and blue side to the peak center at  $2092 \text{ cm}^{-1}$ . The insets for both the concentrations show that the curves at  $2092 \text{ cm}^{-1}$  have a growing term in addition to the population relaxation, while the curves at  $2065 \text{ cm}^{-1}$  decay faster than the curves at  $2073 \text{ cm}^{-1}$ . The linear absorption spectrum of SeCN<sup>-</sup> in water has a tail on the red side due to increased transition dipole moment (non-Condon effect). As the SeCN<sup>-</sup> population within the absorption band was excited by the pump pulse, the SeCN<sup>-</sup> ions with instantaneous frequency at  $2065 \text{ cm}^{-1}$  would be over-pumped while the ions with instantaneous frequency at  $2092 \text{ cm}^{-1}$  would be under-pumped. The result is that spectral diffusion would cause a net flow of population from  $2065 \text{ cm}^{-1}$  to  $2092 \text{ cm}^{-1}$ . At the peak center, this extra population dynamics due to non-Condon effect is balanced out by the input of population from the red side and the output of population to the blue side, and therefore our data analysis of anisotropy decay and population relaxation were performed at the peak center frequency.

In Figure S9, we show that the anisotropy decay curves of each hydrogel sample measured at different frequencies differ only slightly from each other.

## Supporting Tables

**Table S1.** Wobbling-in-a-cone diffusion times for HOD and SeCN<sup>-</sup> in PAAm hydrogels.

Sample	$\tau_c$ (ps) <sup>a</sup>	$\theta_c$ (deg.) <sup>a</sup>	$D_w^{-1}$ (ps) <sup>b</sup>
HOD in H <sub>2</sub> O			
10% PAAm	1.0 ± 0.2	21 ± 1	25 ± 5
25% PAAm	1.4 ± 0.2	28 ± 1	21 ± 4
40% PAAm	1.8 ± 0.2	33 ± 1	21 ± 3
SeCN <sup>-</sup> in D <sub>2</sub> O			
0% PAAm (Bulk Water)	2.0 ± 0.1	21.5 ± 0.4	51 ± 3
5% PAAm	2.7 ± 0.2	29 ± 1	39 ± 3
10% PAAm	2.8 ± 0.2	31 ± 1	36 ± 3
25% PAAm	2.6 ± 0.2	30 ± 1	36 ± 3
40% PAAm	3.0 ± 0.2	29 ± 1	43 ± 3

<sup>a</sup> Reproduced from Table I, main text.

<sup>b</sup> Calculated with Eq. (S6). For HOD, values of  $D_w^{-1}$  averaged across detection frequencies. For SeCN<sup>-</sup>, value is for center of absorption band.

**Table S2.** Characteristic water pool distance scales for hydrogels, equivalent reverse micelle  $d_m$  and  $w_0$  values, and geometric interfacial water fractions for the gels and equivalent RMs.

$T$ (%)	$C_m$ (g/cm <sup>3</sup> )	$d_w$ (nm)	$l_w$ (nm)	$d_m^{\text{gel}}$ (nm) <sup>a</sup>	$w_0^{\text{gel}}$	$f_s^{\text{gel}}$	$f_s^{\text{RM}}$
5	0.05	7.3	13.9	10.6	33	0.02	0.15
10	0.10	4.7	9.3	7.0	20	0.05	0.22
25	0.25	2.4	5.3	3.8	9	0.12	0.39
40	0.40	1.5	3.8	2.6	5	0.22	0.52

<sup>a</sup> Mean of  $d_w$  and  $l_w$ , taken as diameter for corresponding reverse micelle (RM) of equivalent confinement length scale.

**Table S3.** Summary of orientational relaxation of confined water (HOD in H<sub>2</sub>O) in a range of large to small RMs from polarization-selective IR pump-probe results.<sup>34</sup>

$d_m$ (nm)	$w_0$	# Components	$\tau_{\text{core}}$ (ps)	$\tau_{\text{shell}}$ (ps)
17 <sup>a</sup>	37	2, bulk like core	2.6	18
9 <sup>a</sup>	25	2, bulk like core	2.6	18
5.9	16.5	2, bulk like core	2.6	18
4.0	10	2, perturbed core	4.0	26
2.6	5	1	-	30 <sup>b</sup>
1.7	2	1	-	110 <sup>b</sup>

<sup>a</sup>  $w_0$  values outside the range of applicability of Eq. (S20).  $d_m$  values from Moilanen, et. al.<sup>34</sup>

<sup>b</sup> For 1-component regime, shell refers long-time orientational relaxation of entire water pool, in which all molecules are affected by the surfactant interface.

## Supporting Figures

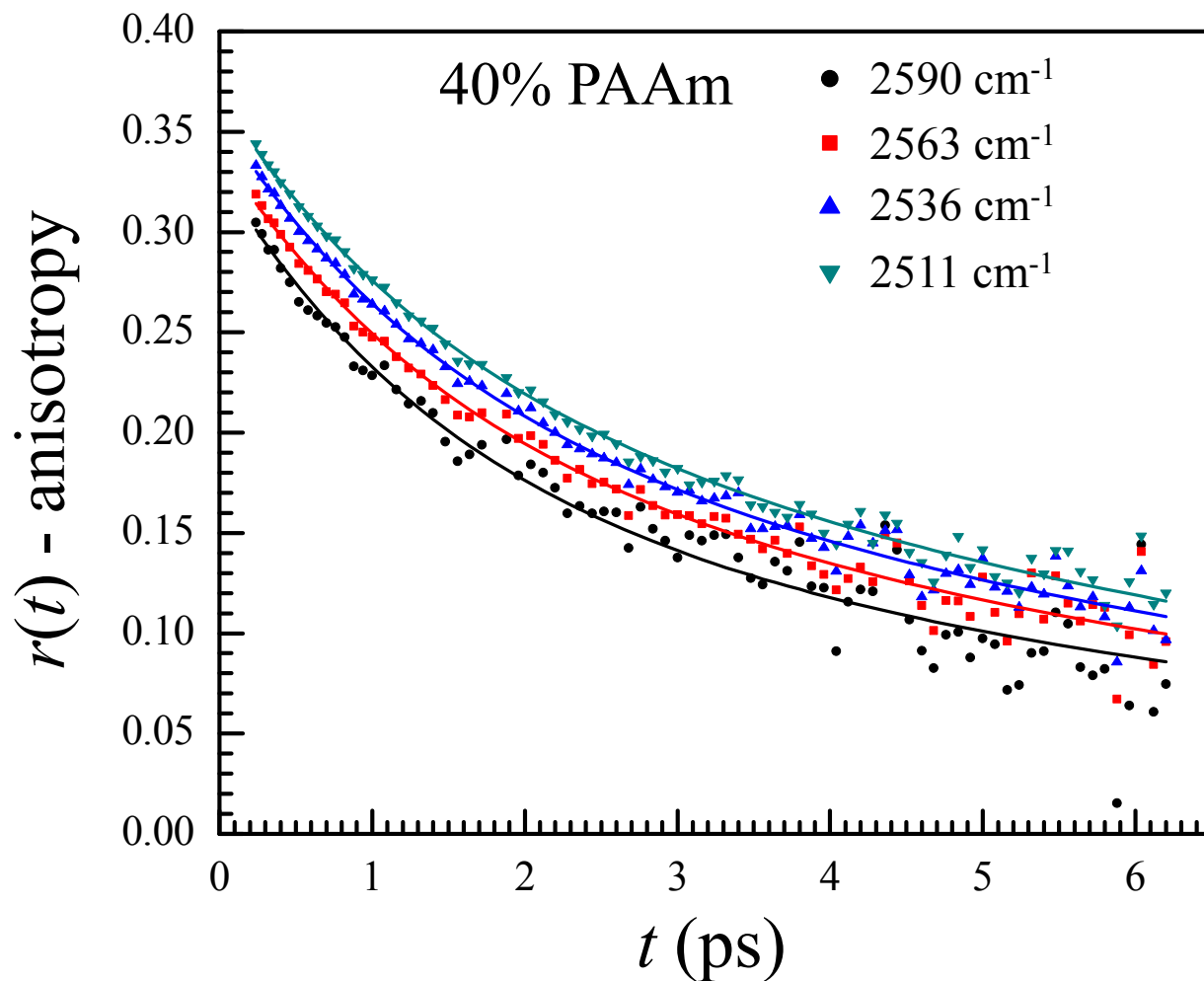


**Figure S1.** Representative anisotropy decays (points) and biexponential fits (solid lines) at 4 detection frequencies for HOD in the  $T = 40\%$  hydrogel. Frequencies range from the absorption peak to the blue edge. The global fits, sharing the time constants at each  $T$  but allowing the amplitudes to freely vary between the different detection frequencies, describe the data extremely well. The fits have similar quality at all frequencies analyzed and for all PAAm concentrations.

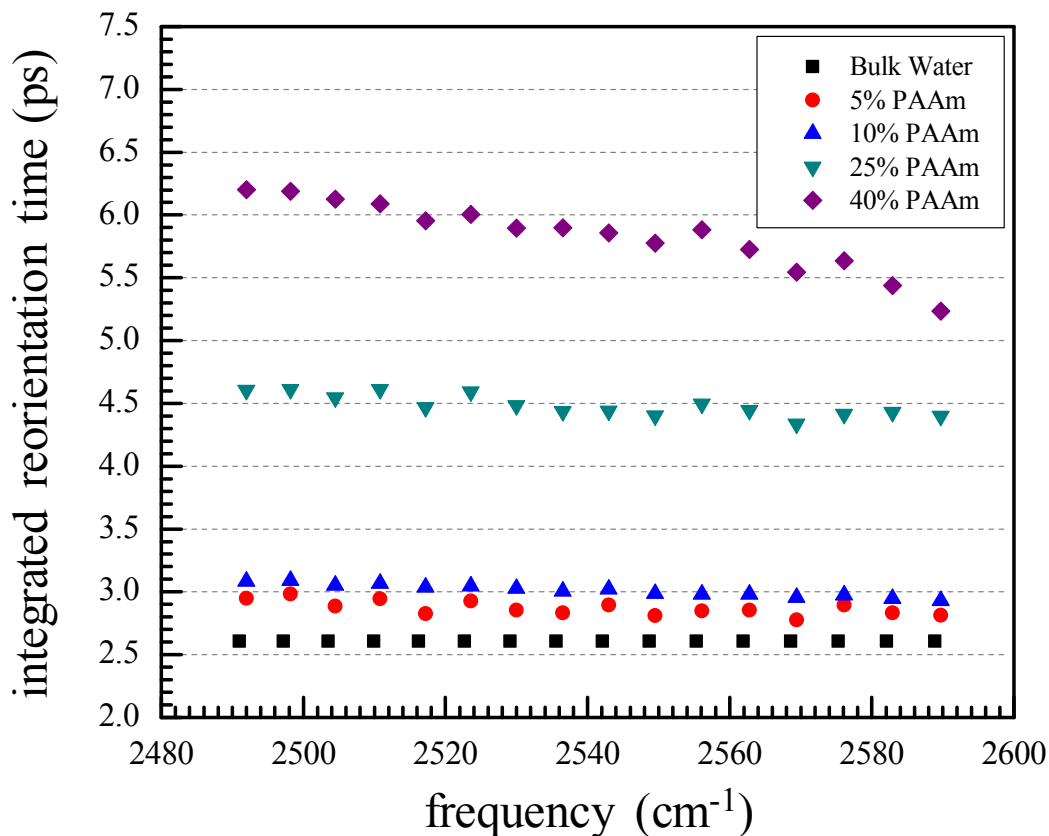


**Figure S2.** Integrated rotational correlation times for the O-D stretch anisotropy,  $r(t) = 0.4C_2(t)$ , measured for

HOD in H<sub>2</sub>O:  $\tau_{\text{cor}} = C_2(0)^{-1} \int_0^\infty C_2(t) dt$ . The correlation time for orientational relaxation is drastically slowed between 10% and 25% *T* concentrations. An additional major slowdown occurs between 25% and 40% PAAm. For all the gels, there is a trend of faster reorientation towards the blue side of the band. This is caused by the larger wobbling cone angles (Figure S4) resulting from weaker H-bonds. The H-bond strength determines the vibrational frequency, with bluer frequencies indicating weaker H-bonds and redder frequencies indicating stronger H-bonds.

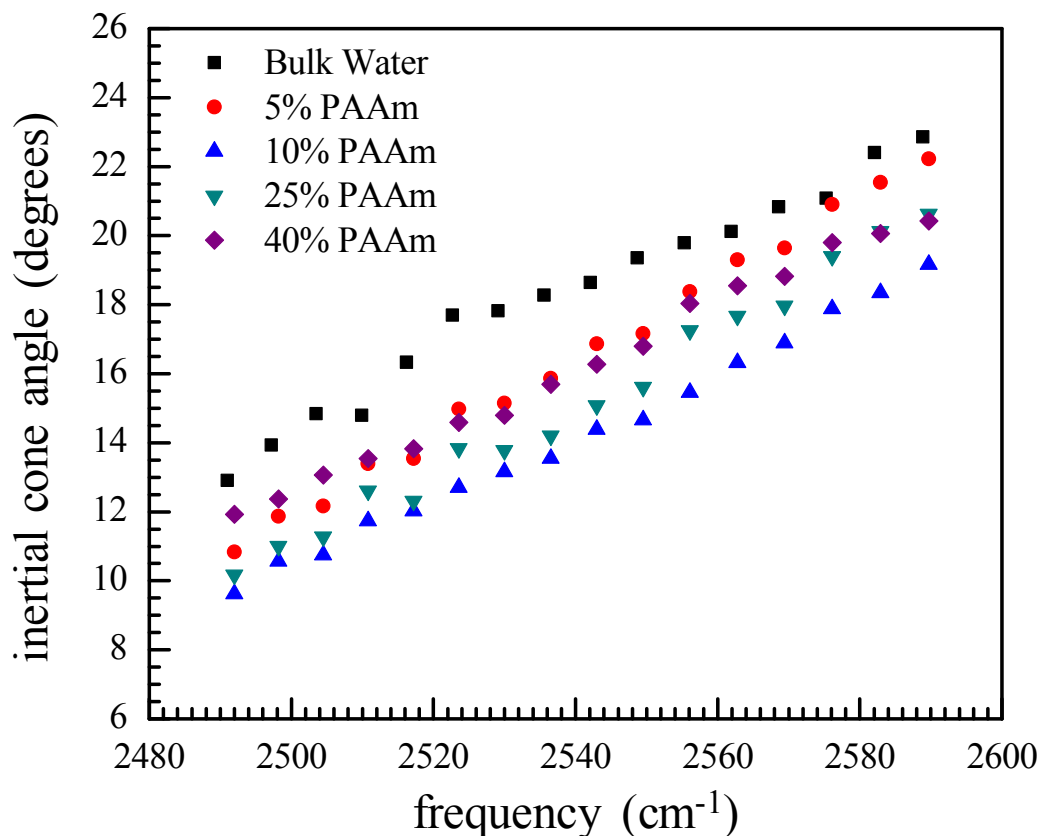


**Figure S3.** Inertial cone angles,  $\theta_{in}$ , for the O-D stretch of HOD in bulk water and all hydrogel concentrations as a function of detection frequency. Though the average cone angle has some spread between PAAm concentrations, the frequency dependence is essentially identical for all samples. More weakly H-bonded O-D oscillators on the blue side have a great deal more inertial rotational freedom on ultrafast timescales ( $< 100$  fs) as compared to those with stronger H-bonds on the red side of the absorption band. The inertial cone angles appear somewhat smaller in the hydrogel samples than in bulk water, which could indicate some confinement effects even on the shortest of time scales. The differences between gel concentrations are not outside the error, however. Uncertainty is between 2 and 6 degrees, with larger error for the smaller cone angles to the red.

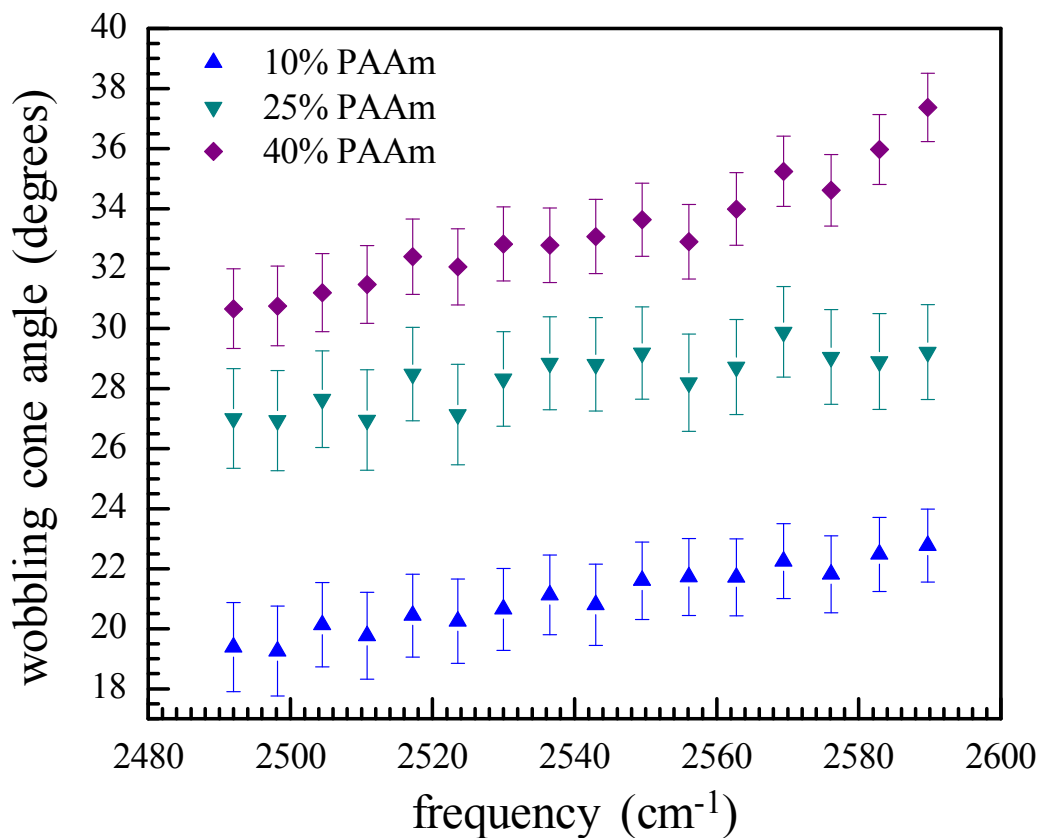


**Figure S4.** Wobbling-in-a-cone half angles,  $\theta_c$ , for  $T = 10\%$ ,  $25\%$ , and  $40\%$  hydrogels as a function of detection frequency. The lowest concentration gel with  $5\%$  PAAm did not have an observable wobbling cone; it was likely too small to allow the additional exponential decay to be detected. Cone angles increase towards the blue edge of the band due to weaker average hydrogen bond strengths allowing more angular space to be sampled. This frequency dependence is the source of the faster integrated correlation times on moving to the blue shown in Figure S2.

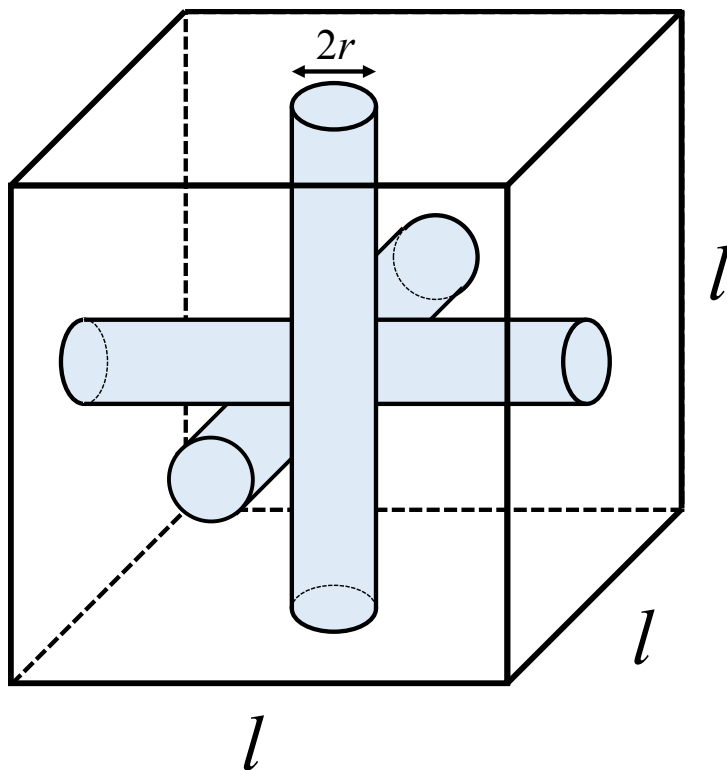


**Figure S5.** Illustration of cubic lattice for estimation of hydrogel pore size. The box is of length  $l$  on each side. Three polymer fibers of radius  $r$  intersect at the center, spanning the length of the box.

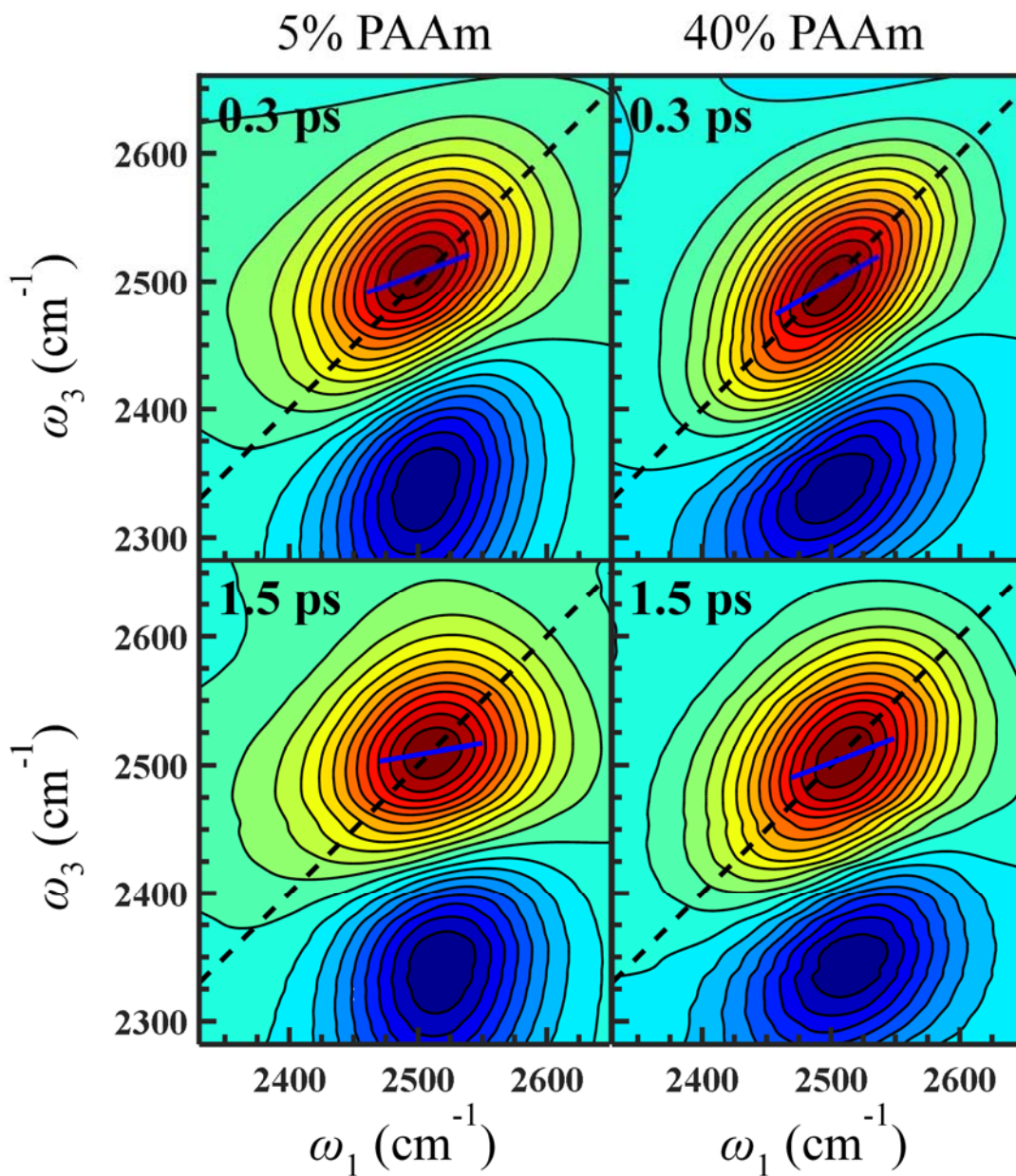


**Figure S6.** 2D IR spectra measured on the O-D stretch of HOD for the 5% and 40% PAAm hydrogels at two waiting times,  $T_w = 0.3$  and 1.5 ps. Black dashed line is the diagonal, while the solid blue line displays the fit to the center line which determines the CLS. The bands change shape with waiting time as single dynamical ensembles.

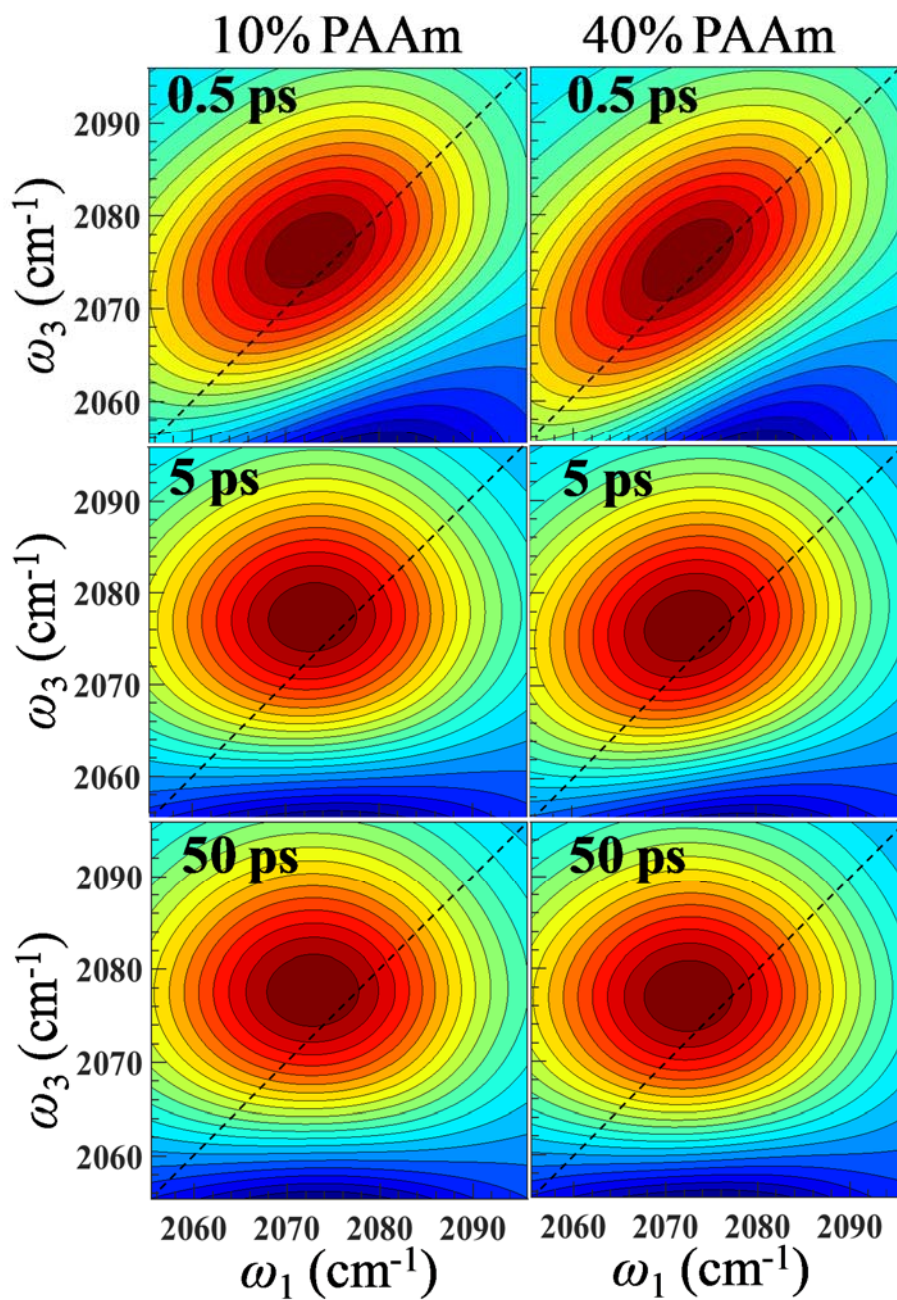


**Figure S7.** 2D IR spectra measured on the nitrile stretch of  $\text{SeCN}^-$  for the 10% and 40% PAAm hydrogels compared at three different waiting times,  $T_w = 0.5, 5$  and  $50$  ps. Black dashed lines are the diagonals.

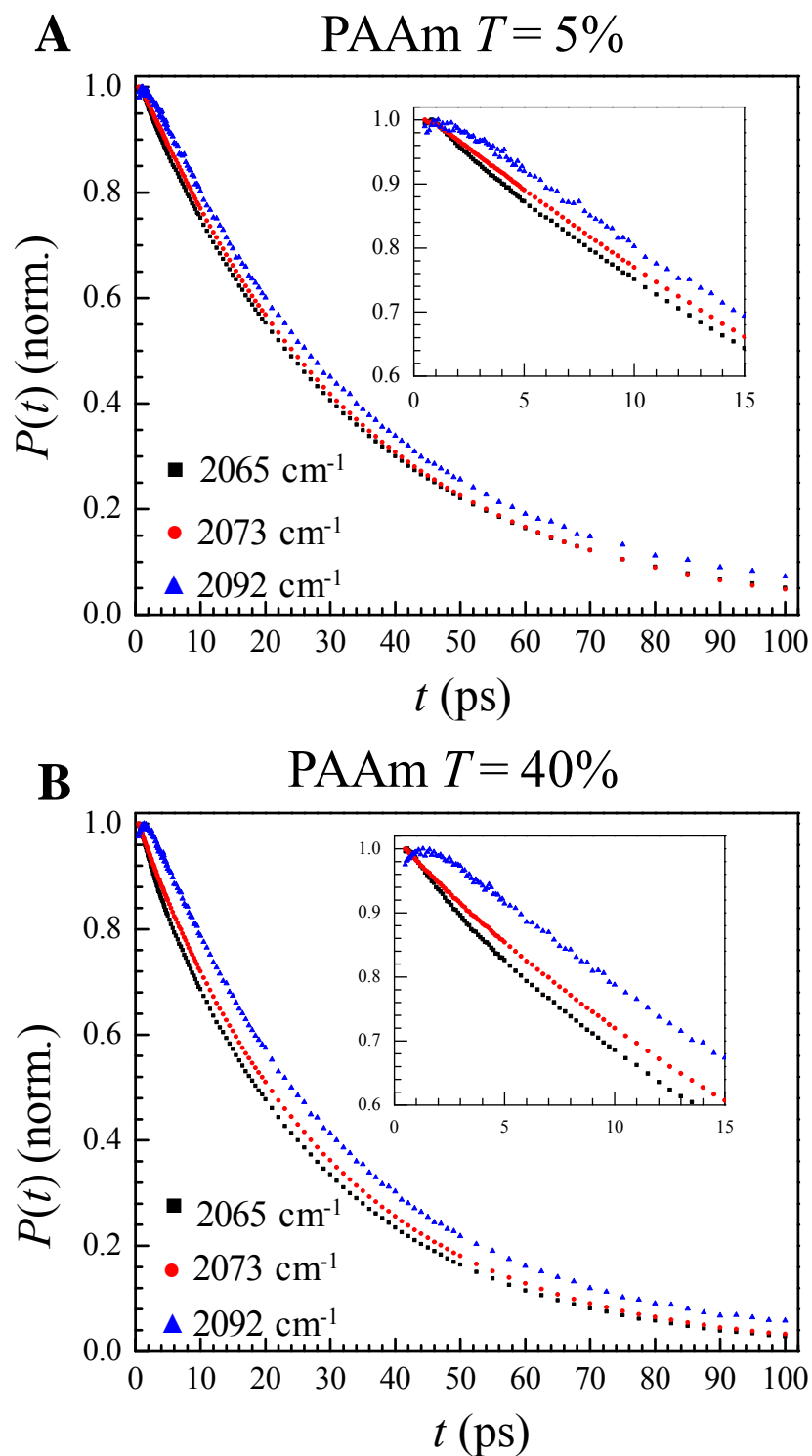


**Figure S8.** Population relaxation of  $\text{SeCN}^-$  measured at different frequencies (peak center, red, and blue of the peak center). The decay curves were normalized to their maximum values for comparison. The insets display data measured at short waiting times with an expanded scale.

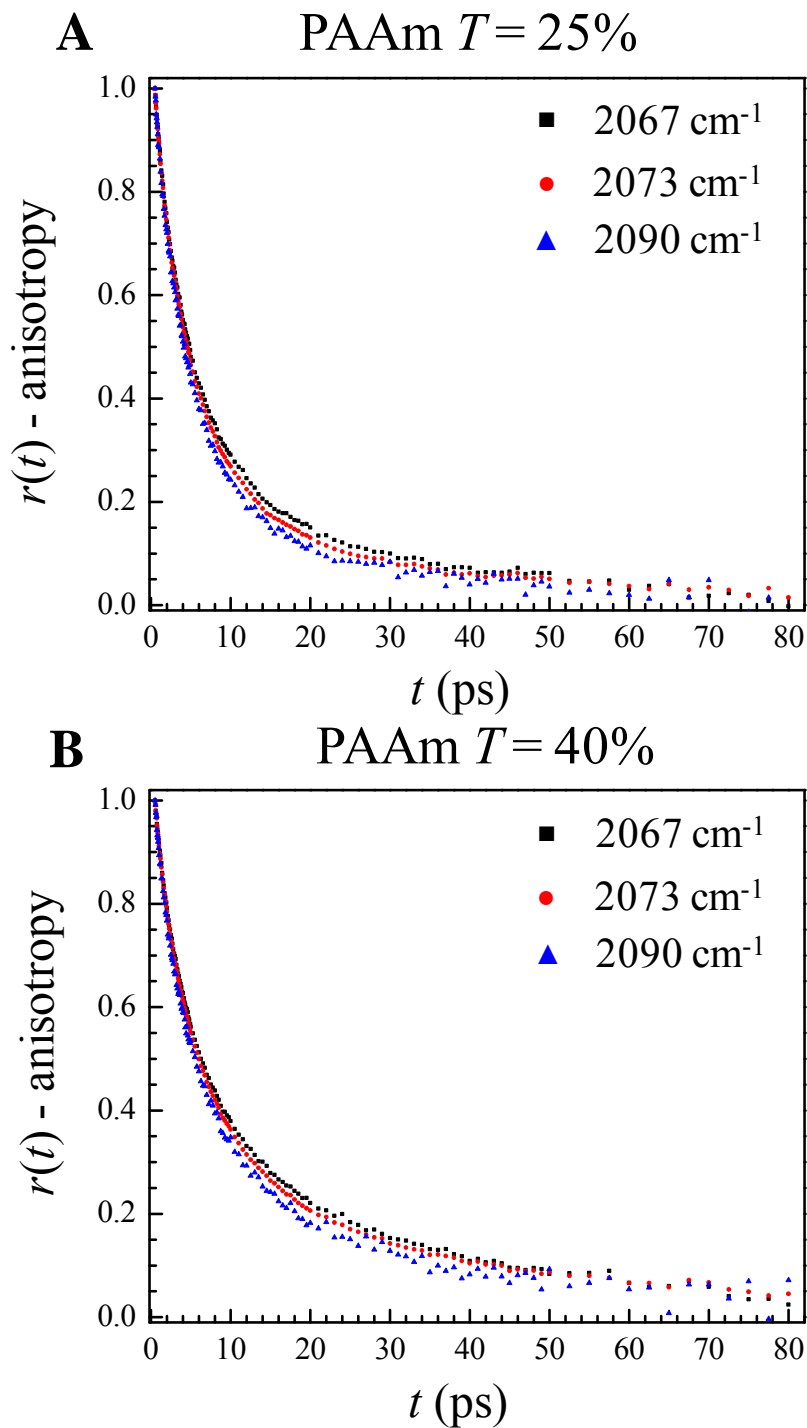


**Figure S9.** Normalized anisotropy decay curves of SeCN<sup>-</sup> measured at different frequencies (peak center, red, and blue of the center). The time dependence is essentially unchanged across frequencies.

## References

- (1) Fenn, E. E.; Wong, D. B.; Fayer, M. D. Water Dynamics in Small Reverse Micelles in Two Solvents: Two-Dimensional Infrared Vibrational Echoes with Two-Dimensional Background Subtraction. *J. Chem. Phys.* **2011**, *134*, 054512.
- (2) Kramer, P. L.; Giammanco, C. H.; Fayer, M. D. Dynamics of Water, Methanol, and Ethanol in a Room Temperature Ionic Liquid. *J. Chem. Phys.* **2015**, *142*, 212408.
- (3) Hamm, P.; Zanni, M. T. *Concepts and Methods of 2D Infrared Spectroscopy*; Cambridge University Press: Cambridge ; New York, 2011.
- (4) Mukamel, S. *Principles of Nonlinear Optical Spectroscopy*; Oxford University Press: New York, 1995.
- (5) Park, S.; Kwak, K.; Fayer, M. D. Ultrafast 2D-IR Vibrational Echo Spectroscopy: A Probe of Molecular Dynamics. *Laser Phys. Lett.* **2007**, *4*, 704-718.
- (6) Rezus, Y. L. A.; Bakker, H. J. On the Orientational Relaxation of HDO in Liquid Water. *J. Chem. Phys.* **2005**, *123*, 114502.
- (7) Steinel, T.; Asbury, J. B.; Zheng, J. R.; Fayer, M. D. Watching Hydrogen Bonds Break: A Transient Absorption Study of Water. *J. Phys. Chem. A* **2004**, *108*, 10957-10964.
- (8) Yan, C.; Thomaz, J. E.; Wang, Y. L.; Nishida, J.; Yuan, R. F.; Breen, J. P.; Fayer, M. D. Ultrafast to Ultraslow Dynamics of a Langmuir Monolayer at the Air/Water Interface Observed with Reflection Enhanced 2D IR Spectroscopy. *J. Am. Chem. Soc.* **2017**, *139*, 16518-16527.
- (9) Yuan, R. F.; Yan, C.; Nishida, J.; Fayer, M. D. Dynamics in a Water Interfacial Boundary Layer Investigated with IR Polarization-Selective Pump-Probe Experiments. *J. Phys. Chem. B* **2017**, *121*, 4530-4537.
- (10) Tan, H.-S.; Piletic, I. R.; Fayer, M. D. Polarization Selective Spectroscopy Experiments: Methodology and Pitfalls. *J. Op. Soc. Am. B: Optical Physics* **2005**, *22*, 2009-2017.
- (11) Kramer, P. L.; Nishida, J.; Giammanco, C. H.; Tamimi, A.; Fayer, M. D. Observation and Theory of Reorientation-Induced Spectral Diffusion in Polarization-Selective 2D IR Spectroscopy. *J. Chem. Phys.* **2015**, *142*, 184505.
- (12) Kramer, P. L.; Nishida, J.; Fayer, M. D. Separation of Experimental 2D IR Frequency-Frequency Correlation Functions into Structural and Reorientation-Induced Contributions. *J. Chem. Phys.* **2015**, *143*, 124505.

- (13) Kinoshita, K.; Ikegami, A.; Kawato, S. On the Wobbling-in-Cone Analysis of Fluorescence Anisotropy Decay. *Biophys. J.* **1982**, *37*, 461-464.
- (14) Kinoshita, K.; Kawato, S.; Ikegami, A. Theory of Fluorescence Polarization Decay in Membranes. *Biophys. J.* **1977**, *20*, 289-305.
- (15) Lipari, G.; Szabo, A. Effect of Librational Motion on Fluorescence Depolarization and Nuclear Magnetic-Resonance Relaxation in Macromolecules and Membranes. *Biophys. J.* **1980**, *30*, 489-506.
- (16) Wang, C. C.; Pecora, R. Time-Correlation Functions for Restricted Rotational Diffusion. *J. Chem. Phys.* **1980**, *72*, 5333-5340.
- (17) Tan, H.-S.; Piletic, I. R.; Fayer, M. D. Orientational Dynamics of Water Confined on a Nanometer Length Scale in Reverse Micelles. *J. Chem. Phys.* **2005**, *122*, 174501.
- (18) Ramasesha, K.; Roberts, S. T.; Nicodemus, R. A.; Mandal, A.; Tokmakoff, A. Ultrafast 2D IR Anisotropy of Water Reveals Reorientation During Hydrogen-Bond Switching. *J. Chem. Phys.* **2011**, *135*, 054509.
- (19) Spry, D. B.; Goun, A.; Glusac, K.; Moilanen, D. E.; Fayer, M. D. Proton Transport and the Water Environment in Nafion Fuel Cell Membranes and AOT Reverse Micelles. *J. Am. Chem. Soc.* **2007**, *129*, 8122-8130.
- (20) Lipari, G.; Szabo, A. Model-Free Approach to the Interpretation of Nuclear Magnetic-Resonance Relaxation in Macromolecules. 1. Theory and Range of Validity. *J. Am. Chem. Soc.* **1982**, *104*, 4546-4559.
- (21) Deeg, F. W.; Stankus, J. J.; Greenfield, S. R.; Newell, V. J.; Fayer, M. D. Anisotropic Reorientational Relaxation of Biphenyl: Transient Grating Optical Kerr Effect Measurements. *J. Chem. Phys.* **1989**, *90*, 6893.
- (22) McMorro, D.; Lotshaw, W. T.; Kenney-Wallace, G. A. Femtosecond Optical Kerr Studies on the Origin of the Nonlinear Response in Simple Liquids. *IEEE J. Quantum Electron.* **1988**, *24*, 443-454.
- (23) Sturlaugson, A. L.; Arima, A. Y.; Bailey, H. E.; Fayer, M. D. Orientational Dynamics in a Lyotropic Room Temperature Ionic Liquid. *J. Phys. Chem. B* **2013**, *117*, 14775-14784.
- (24) Sturlaugson, A. L.; Fruchey, K. S.; Fayer, M. D. Orientational Dynamics of Room Temperature Ionic Liquid/Water Mixtures: Evidence for Water-Induced Structure and Anisotropic Cation Solvation. *J. Phys. Chem. B* **2012**, *116*, 1777-1787.

- (25) Ogston, A. G. The Spaces in a Uniform Random Suspension of Fibres. *Trans. Faraday Soc.* **1958**, *54*, 1754-1757.
- (26) Holmes, D. L.; Stellwagen, N. C. Estimation of Polyacrylamide Gel Pore Size from Ferguson Plots of Normal and Anomally Migrating DNA Fragments. I. Gels Containing 3 % N, N'-Methylenebisacrylamide. *Electrophoresis* **1991**, *12*, 253-263.
- (27) Holmes, D. L.; Stellwagen, N. C. Estimation of Polyacrylamide Gel Pore Size from Ferguson Plots of Linear DNA Fragments. II. Comparison of Gels with Different Crosslinker Concentrations, Added Agarose and Added Linear Polyacrylamide. *Electrophoresis* **1991**, *12*, 612-619.
- (28) Fawcett, J. S.; Morris, C. J. O. R. Molecular-Sieve Chromatography of Proteins on Granulated Polyacrylamide Gels. *Sep. Sci.* **1966**, *1*, 9-26.
- (29) Chrambach, A.; Rodbard, D. Polyacrylamide Gel Electrophoresis. *Science* **1971**, *172*, 440-451.
- (30) Wypych, G. PAAm Polyacrylamide. In *Handbook of Polymers (Second Edition)*; ChemTec Publishing, 2016; pp 254-256.
- (31) Kinugasa, T.; Kondo, A.; Nishimura, S.; Miyauchi, Y.; Nishii, Y.; Watanabe, K.; Takeuchi, H. Estimation for Size of Reverse Micelles Formed by AOT and SDEHP Based on Viscosity Measurement. *Coll. and Surf. A - Physicochem. and Eng. Aspects* **2002**, *204*, 193-199.
- (32) Zulauf, M.; Eicke, H. F. Inverted Micelles and Microemulsions in the Ternary System H<sub>2</sub>O/Aerosol-OT/Isooctane as Studied by Photon Correlation Spectroscopy. *J. Phys. Chem.* **1979**, *83*, 480-486.
- (33) Moilanen, D. E.; Fenn, E. E.; Wong, D.; Fayer, M. D. Water Dynamics at the Interface in AOT Reverse Micelles. *J. Phys. Chem. B* **2009**, *113*, 8560-8568.
- (34) Moilanen, D. E.; Fenn, E. E.; Wong, D.; Fayer, M. D. Water Dynamics in Large and Small Reverse Micelles: From Two Ensembles to Collective Behavior. *J. Chem. Phys* **2009**, *131*, 014704.
- (35) Franks, F. *Water: A Comprehensive Treatise*; Plenum Press, New York, London, 1972; Vol. 1.

- (36) Kwak, K.; Park, S.; Finkelstein, I. J.; Fayer, M. D. Frequency-Frequency Correlation Functions and Apodization in Two-Dimensional Infrared Vibrational Echo Spectroscopy: A New Approach. *J. Chem. Phys.* **2007**, *127*, 124503.
- (37) Kwak, K.; Rosenfeld, D. E.; Fayer, M. D. Taking Apart the Two-Dimensional Infrared Vibrational Echo Spectra: More Information and Elimination of Distortions. *J. Chem. Phys.* **2008**, *128*, 204505.
- (38) Guo, Q.; Pagano, P.; Li, Y.-L.; Kohen, A.; Cheatum, C. M. Line Shape Analysis of Two-Dimensional Infrared Spectra. *J. Chem. Phys.* **2015**, *142*, 212427.
- (39) Schmidt, J. R.; Corcelli, S. A.; Skinner, J. L. Pronounced Non-Condon Effects in the Ultrafast Infrared Spectroscopy of Water. *J. Chem. Phys.* **2005**, *123*, 044513.
- (40) Yamada, S. A.; Thompson, W. H.; Fayer, M. D. Water-Anion Hydrogen Bonding Dynamics: Ultrafast IR Experiments and Simulations. *J. Chem. Phys.* **2017**, *146*, 234501.